A constitutive model for homogenized solid oxide cell contacts with dimensional tolerances

Ralston Pinto[1,3], Fabian Welschinger[1], Nils Giesselmann[1], Holger Reinshagen[1], and Norbert H. Menzler[2,3]

[1]Robert Bosch GmbH, Bamberg, Germany
[2]Forschungszentrum Jülich GmbH, Institute of Energy and Climate Research, IEK-1: Materials Synthesis and Processing, Jülich, Germany
[3]RWTH Aachen, Institute of Mineral Engineering, Aachen, Germany
*correspondence to:

January 30, 2024

Abstract

Dimensional tolerances are a primary concern during manufacturing of solid oxide cells. Tolerances make metallic interconnects sensitive to electrical contacting which highly influences the overall stack performance. Therefore, the force applied to a solid oxide cell stack to establish electrical contact is very crucial. Variability of the height dimension at interconnect contacts may cause non-uniform force distribution and large plastic deformation on some contacts resulting in local damage. This phenomenon may be studied using Finite Element Methods. However, due to geometrically complex designs of interconnects, high-fidelity simulations on stack level resolving the interconnect geometry explicitely are computationally very expensive and cannot be used to study the aforementioned challenges within appropriate time frames. To tackle this dimensional scale bridging problem, in this work, concepts of computational homogenization techniques are investigated to make stack level simulations more efficient that allow for a detailed analysis of the stacking process. The focus of this work is to create a Finite Element framework to understand the effects of heterogenous height tolerances of contacts using the homogenization approach during mechanical pressing. This in turn gives an understanding of its influence on electrical contacting and mechanical deformation of every contact during a stacking process. On the stack level, an effective, anisotropic elastoplastic material model for the interconnect is formulated adding novel features called *offset strain* and *coating strain*. The former allows to precisely simulate dimensional tolerances at low computational cost and the latter considers an additional deformation mechanism of a soft coating material in the interconnect. On the individual contact level, high-fidelity simulations of the fully resolved interconnects are carried out to determine their homogenized mechanical behavior. These insights are then used to calibrate the effective macroscopic model which can be used to effectively optimize the stacking force distribution for an optimal contacting configuration with minimum deformation of the interconnect contacts.

Keywords: Multiscaling of interconnects; Homogenization for solid oxide cell stack; stack contacting; contact modelling

1 Introduction

1.1 State of the art

There has been a lot of development in fuel and electrolysis cell technology over the past few decades. The current challenge is to bring this technology to production by reducing costs without loss of efficiency and reliability. Dimensional tolerances during production create variance in the cell performances in a stack which could lead to critical problems during operation. For planar solid oxide cells (SOCs), the interconnect is very sensitive to dimensional tolerances. The functional role of the interconnect is to separate the air and fuel compartments, and to form electrical contacts between layers. Dimensional tolerances on an interconnect may affect fuel distribution creating hot spots and cause inefficient electrical contact between layers. Tolerances on the interconnect contacts play a significant role in electrical conductivity. Specifically, varying height tolerances at these contacts in the range of a few tens of microns may lead to loss of performance. The Finite Element Method (FEM) is one approach to understand forces required during stacking of fuel cells to establish optimal contacting of the interconnects. However, conventional simulation methods fully resolving the interconnects in the entire assembly require large computation times caused by the immense high mesh resolution of geometrically complex contacts and the large number of repeating units in a stack, see Wu et al. [1]. Among others, Navasa et al. [2] have recently studied computational homogenization techniques exploiting the periodically repeating structure of the interconnect design. This approach could be used to get a high order of accuracy in combination with practical computation times for stack level simulations. As general structure for computational inelastic homogenization, a conventional full mesh model referred to as the *high-fidelity model* is homogenized to obtain stress-strain relations for several load cases. A simplified block model referred to as the *effective model* can be fitted on to the homogenized responses for the corresponding load cases. The general idea is to replace the geometric complexities which may require a high mesh resolution to an equivalent material response with a coarser resolution, reducing the computation time by several orders of magnitude. For this work, the directions in the plane of the interconnect is referred to as the *in-plane* direction and the direction of stacking is referred to as the *out-of-plane* direction.

Several homogenization schemes have been developed over the past decades along with constitutive models for elastic-inelastic solids, e.g., Simo & Hughes [3] and Lemaitre & Chaboche [4]. So, it is worthwhile to first identify the suitable effective model for the current application. Solid oxide cells need to be stacked together and it is necessary to make sure that there is sufficient contact pressure and area between layers. So, the stack may be subjected to large forces which may not be evenly distributed, onsetting plasticity in certain areas. Therefore, an inelastic constitutive behavior is required for the effective model. Moreover, it is observed that the in-plane stiffness is significantly greater than the out-of-plane stiffness for such kind of structures, see Molla et al. [5] and Tsuda et al. [6]. This is because its corrugated shape, designed to form channels for passage of air and fuel, collapse rather easily out-of-plane than deform in-plane. Therefore, an anisotropic effective model has been suggested. In the above mentioned studies, the need for compressible plasticity has been expressed while homogenizing similar structures. This means that, the onset of plasticity should render a non-isochoric material response. This is because, the out-of-plane deformation shows negligible in-plane distortion during the collapse of these channels. In summary, a compressible anisotropic elastoplastic effective model would be ideal to model interconnect contacts.

In general, metal plasticity models are based on Von Mises theory combined with some hardening effects which is associative in nature, meaning that, plastic deformation is driven purely by deviatoric stresses and show an isochoric material response. However, in recent years, there have been non-associative models used for geomaterials like soil and rocks which essentially show a non-isochoric behavior, e.g., Ulloa et al. [7]. The key ingredients for any elastoplastic model are: a yield surface that bound the elastic domain with a yield function and a set of evolution equations to update the internal variables called the flow rule. For associative plasticity, the internal variables are updated keeping their rate of change normal to the yield surface, i.e., normality is always implied by the flow rule. However, for non-associative plasticity, normality is no longer implied and there is the need of a more generalized flow rule derived from a plastic potential which may differ from the yield function. This could give non-associative models a purely phenomenological perspective, where the second law of thermodynamics is not necessarily enforced and a variational structure may not be formed. Therefore, for the current application, an associative model is the better choice, however, a non-isochoric behavior needs to be maintained in the plastic domain.

One approach to model non-isochoric plasticity, while maintaining a variational structure was formulated in the work of Deshpande & Fleck [8] when modelling the isotropic behavior of aluminum alloy foams. This work uses a plastic Poission's ratio while assuming an associated flow rule and introduces plastic compressibility into the Von Mises framework of elastoplastic material models. This idea was then extended for modelling compressive behavior of metallic sandwich core structures in the work of Xue & Hutchinson [9] for the rate-independent anisotropy. In this work, the authors created a dependence of the effective yield stress on hydrostatic stress components by altering Hill's criteria and formulated an algorithm for anisotropic elastoplasticity based on this modified Hill's criteria. Later, Tsuda et al. [6] formulated a rate-dependent steady state extension of the model by Xue & Hutchinson [9] to model the homogenized elastic–viscoplastic behavior of plate-fin structures. The model proposed in this work uses the framework of Tsuda et al. [6] and introduces new modelling equations which can be adapted for any kind of elastoplastic model.

1.2 Contributions

Tsuda et al. [6], Navasa et al. [2] and Molla et al. [5] use computational homogenization methods to obtain properties of a periodically repeating structure. The homogenized properties were set as a reference to fit an effective model which represented the high-fidelity model in all respect. For the case of interconnect contacts, the variability in the *height dimension* in the out-of-plane direction was observed to pose a significant issue for electrical contacting. In this work, the homogenized stress-strain responses of interconnect contacts with two different height dimensions were first obtained. A material model is developed for compressible anisotropic rate-dependent plasticity that represents these dimensional tolerances as a material response. This was done by introducing a novel idea of so-called *offset-strain* in the principle direction of these height tolerances. Analoguously, this idea is further extended to model the behavior of an interconnect which contains a porous coating layer. The effective properties of these coated interconnects were highly nonlinear and otherwise difficult to model using conventional material models.

In Section 2, a design to work with is first introduced and the basic concepts of periodic homogenization are discussed. Then, the homogenized responses are obtained by loading a representative volume of the interconnect in the principle directions. In Section 3, interconnect contacts with dimensional tolerances are homogenized and the concepts of offset- and coating-strains are discussed. Besides the extended kinematics, constitutive equations are then formulated in the framework of rate-dependent compressible anisotropic elastoplasticity. Section 4 shows the validation of the constitutive model by testing it with its corresponding high-fidelity simulations. Lastly, a layout which relates the output from the effective model to the contact pressure in a high figelity model is discussed and gives a direct theoretical relation to the electrical contacting. Zhu & Ghezel-Ayagh [10] and Kennouche at al. [11] discuss the relation and significance of contact pressure to the electrical performance and is not looked at in this work.

2 High-fidelity model of interconnect contact

2.1 Description of the model

The schematic representation of a planar SOC referring to a patent from Ceres Power Limited [12] is shown in Figure 1. One repeat unit consists of an interconnect, metallic substrate and anode-electrolyte-cathode layers. The holes on the metallic substrate allow the passage of fuel through the electrolyte and the gaskets ensure no leakage of air into the fuel stream. The interconnect has an indented structure which contacts the next layer allowing flow of electric current. Therefore, it is necessary to ensure an optimal contact pressure for high efficiency of electron flow. These contacts also create channels that separate air and fuel, so it is necessary that the height of these contacts are evenly maintained to ensure efficient air-fuel distribution in a cell. Because of its corrugated design, the interconnect is generally the least stiff component during stack compression. Most other components are solid, flat and see no plastic deformation. Therefore, the other components are represented as a rigid plate in this study as was done in the work of Molla et al. [5]. The significance of electrical contacting lies in the active area of the interconnect, therefore, for simplicity, only the active area is considered in this work. The dimensions of an ideal interconnect contact is shown in Figure 1.[1] Crofer 22 APU by VDM Metals is a commonly used material for the metallic interconnect, see Molla et al. [5], Abdoli et al. [13] and Shen et al. [14]. The elastic and plastic properties were taken from the material data sheet [15] and are summarized in Table 1.

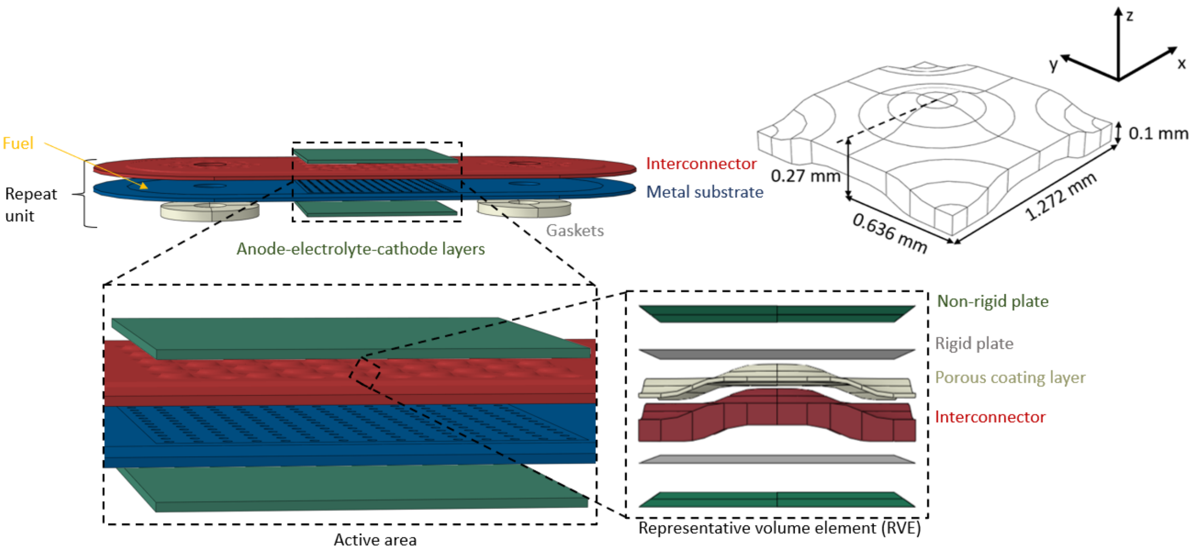

Figure 1: Schematic of a standard repeating fuel cell unit and definition of the representative volume element.

---

[1] Geomerty and material data used in this work may be scaled/altered so that it is not specific to any manufacturer. However, the effects seen in the curves correspond to reality.

Table 1: Material data for metallic interconnect according to Abdoli et al. [13].

Young's Modulus (MPa)	Poisson's ratio (-)
220000	0.3
Yield stress (MPa)	Plastic strain (-)
250	0
277	0.002
365	0.01

The metallic interconnect is usually coated with a coating layer. After some indentation experiments, the material data for the coating layer was evaluated. The pressure-closure data for the coating is shown in Table 2 and is modelled with the gasket material model in ABAQUS. The thickness of the coating was taken to be 0.02 mm. After a mesh convergence study, C3D8 elements were chosen for the metallic interconnect. GK3D8N elements were chosen for the coating material because its exponential stiffness could be closely depicted using gasket material properties. Finite element calculations were done using the commercially available software package ABAQUS.

Table 2: Pressure-closure relation for coating layer.

Pressure (MPa)	Closure (mm)
0	0
0.2	5.00E-07
4.4	0.00014
5	0.00062
11.04	0.002225
16.8	0.00428
33.36	0.00794
128.91	0.01134
374.32	0.01458
795.066	0.0169
1419.986	0.01858
1913.878	0.0191
2878.67	0.02

2.2 Computational homogenization

The interconnect geometry is a periodically repeating structure in the active area as described in Figure 1. The representative unit volume primarily comprised of one interconnect contact and its coating. For homogenization in the out-of-plane loading direction, these components were sandwiched between rigid plates, to enforce the assumption that other components showed no deformation as discussed in Section 2.1. Discrete rigid elements are generally limited when setting kinematic equation constraints at its nodes, therefore, this geometry was again sandwiched between non-rigid plates for a consistent set of periodic boundary conditions, see Figure 1. The non-rigid plates were only placed to link the corner, edge and face nodes at the top and bottom faces and showed no contribution to the stress-strain response. For in-plane loading, the plates were not included for the kinematic equation constraints. Periodic boundary conditions were applied to the representative unit volume referring to the work of Li et al. [16] and Li [17]. Based on their work, kinematic equation constraints were set up on edges, corners and faces of the unit cell. These were linked to 6 reference nodes called *key degrees of freedom*[1][2] in directions (xx, yy, zz, xy, yz, xz). In this approach, nodal displacements at these key degrees of freedom are equal to the homogenized strains in the corresponding direction. Concentrated forces at the key degrees of freedom have dimensions equivalent to force times length. The homogenized stress is, therefore, equal to the concentrated force at the key degrees of freedom divided by the volume of the unit cell and has been proven in a rigorous derivation in [17]. This approach eliminates the need to calculate average stresses and strains in a post-processing step, provided that, the kinematic equations are in the form stated in Appendix A.

2.3 High-fidelity response

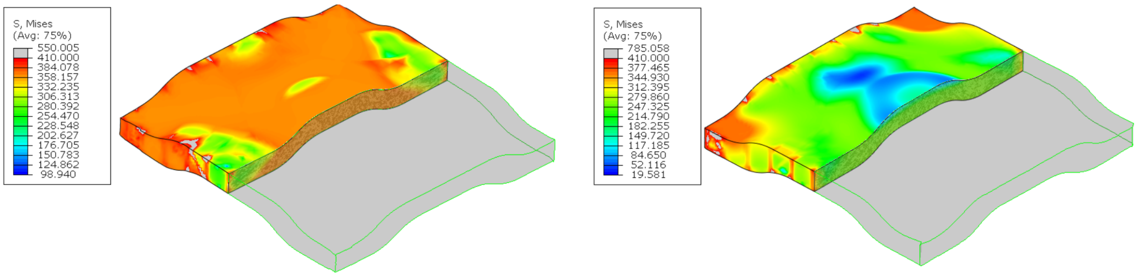

(a) In-plane normal load $\varepsilon_{xx} = \varepsilon_{yy}$

(b) In-plane shear load ε_{xy}

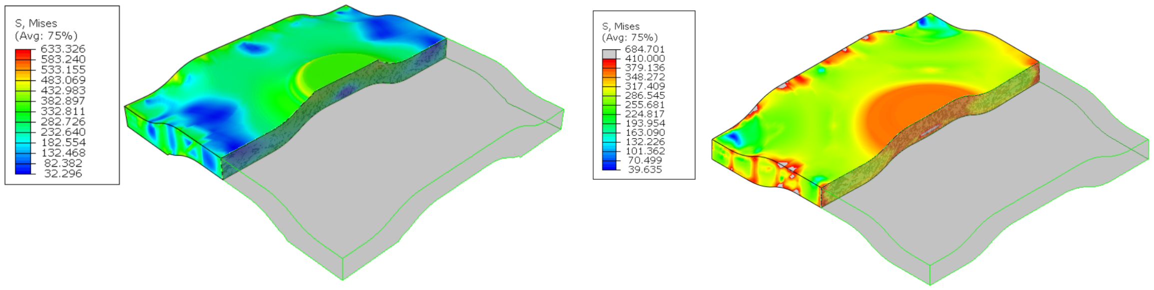

(c) Out-of-plane shear load $\varepsilon_{xz} = \varepsilon_{yz}$

(d) Out-of-plane normal load ε_{zz}

Figure 2: Von Mises stress distributions in the high fidelity interconnect model.

Due to in-plane symmetry of the geometry, the elastoplastic stress-strain responses were computed for four loading cases only. The concentration of Von Mises stress on the cross section of the metallic interconnect contact for these loading cases are shown in Figure 2. Figure 2(a) shows the case for

---

[1] Based on the coupling constraints in Appendix-A, the nodal displacement at the key degree of freedom in any direction (dir) is $u^{cd}_{dir} = u_{dir}/l_{dir}$ and is equivalent to the homogenized strain component in that direction.

[2] Similarly, the nodal force at the key degree of freedom in any direction (dir) is $f^{cd}_{dir} = f_{dir} \times l_{dir}$. Once divided by the volume of the RVE, corresponds to the homogenized stress component in that direction.

uniaxial normal loading in the in-plane direction (xx, yy). Similarly, Figure 2(d) shows the uniaxial normal loading case in the out-of-plane direction (zz). Figure 2(b) and Figure 2(c) show shear loading cases in the in-plane (xy) and out-of-plane (xz, yz) directions. The results and observations for all cases are summarized in Figure 3. The stress-strain responses showed significant anisotropy between in-plane and out-of-plane loading directions. Figure 3(a) shows that the yield stress in the out-of-plane direction was about one order of magnitude lower than the in-plane direction. This means that the interconnect contacts were significantly stiffer in-plane, however, there is no primary loading in this direction during stacking. Another parameter is the volume dilation during uniaxial loading. This can be seen by plotting

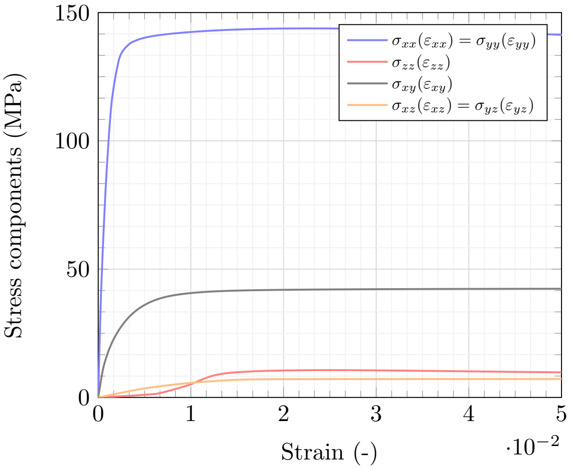

(a) Stress-strain responses for normal and shear loading in the in-plane and out-of-plane direction.

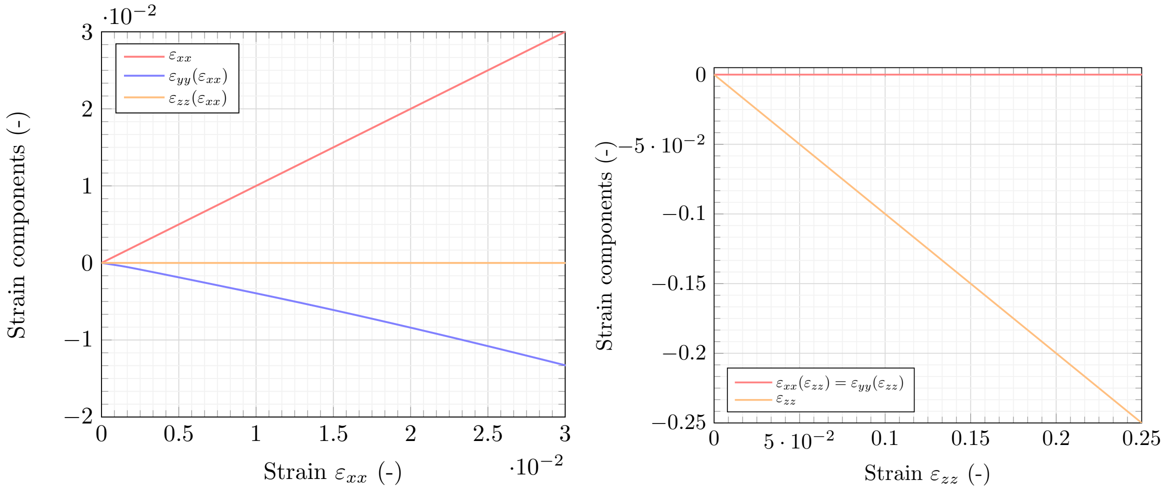

(b) Strain components $\varepsilon_{xx}(\varepsilon_{xx})$ and $\varepsilon_{yy}(\varepsilon_{xx})$ as a result of a normal in-plane strain driver ε_{xx}.

(c) Strain components $\varepsilon_{xx}(\varepsilon_{zz})$ and $\varepsilon_{yy}(\varepsilon_{zz})$ as a result of a normal out-of-plane strain driver ε_{zz}.

Figure 3: Results of computational homogenization

the driving strain with the other strain components in a uniaxial normal loading in Figure 3. Figure 3(b) shows the corresponding strains $\varepsilon_{yy}(\varepsilon_{xx})$ and $\varepsilon_{zz}(\varepsilon_{xx})$ resulting from an in-plane normal loading strain ε_{xx} and Figure 3(c) shows the corresponding in-plane strains $\varepsilon_{xx}(\varepsilon_{zz})$ and $\varepsilon_{yy}(\varepsilon_{zz})$ as a consequence of an out-of-plane normal loading strain ε_{zz}. Figure 3(c) suggests that the interconnect contact collapses without significant in-plane expansion indicating the need for an elastoplastic effective model of a non-isochoric nature. As another observation, depicted in Figure 3(a), the normal out-of-plane loading ε_{zz}

has an initial nonlinear stress response in the out-of-plane stress component $\sigma_{zz}(\varepsilon_{zz})$, which characterizes the influence of the coating layer. This behavior is crucial because it is in the direction of primary loading during the stacking process.

3 Effective model for interconnect

High fidelity simulations are computationally expensive due to the high mesh resolution required for the corrugated interconnect design and the number of repeating units in an SOC stack. The computational effencicy can be increased by replacing the high fidelity repeating geometry with one single brick element of equivalent material behavior who's volume is equal to that of the repeat unit. This reduces the number of elements to one per interconnect contact and significantly reduces the simulation time by several orders of magnitude. Such kind of a model reduction simplifies the problem by converting geometric complexities into non-linear material responses which significantly reduces simulation time while maintaining necessary accuracy.

3.1 Model requirements

The observations in Section 2.3 indicate that an anisotropic effective elastoplastic model is required that considers i) volumetric compressibility, ii) the non-linear irreversible deformation of the soft coating layer and iii) the variability in contact heights. Figure 4(a) and Figure 4(b) show contacts with a difference of 25 μm in their height dimensions and are loaded uniaxially in the out-of-plane direction. Keeping the effective height of the RVE constant, i.e., the distance between top and bottom plates, the homogenized stresses for the short contact σ_{zz}^{sc} and the tall contact σ_{zz}^{tc} are plotted in Figure 4(c). The shorter interconnect

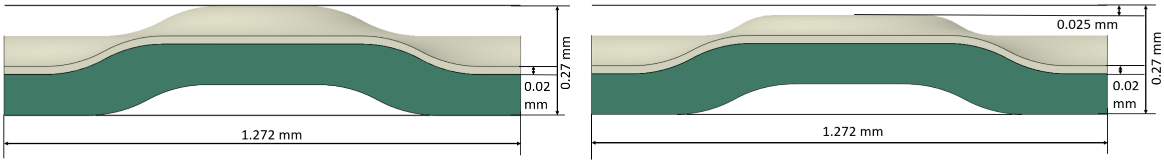

(a) Tall contact with coating.

(b) Short contact with coating.

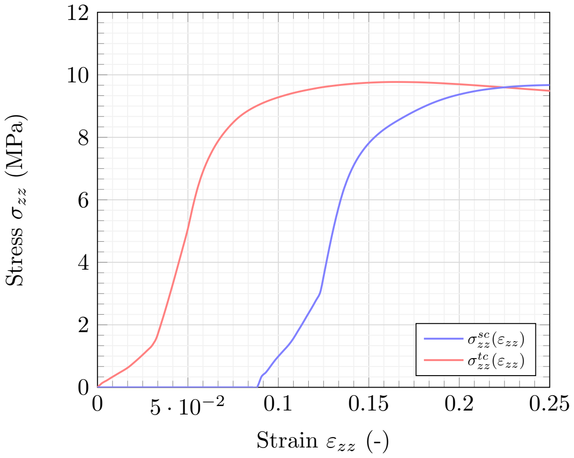

(c) Homogenized normal stress-strain responses.

Figure 4: Impact of height tolerances in interconnect contacts on the homogenized stress-strain response.

contact shows an offset of the stress-strain response on the strain axis and can be interpreted as a zone of zero stiffness until it contacts the plate above. This offset is due to the missing 25 μm height dimension in Figure 4(b). This means that the geometric tolerances at individual contacts in the high-fidelity model can be represented in the form of a material response in the effective model. This is done by introducing a parameter called *offset-strain* which is the strain corresponding to the difference between the height dimension of the representative unit cell and of the measured interconnect contact.

3.2 Basic kinematics and state variables

In a small strain setting the total strain $\boldsymbol{\varepsilon}$ is additively decomposed into

$$\boldsymbol{\varepsilon} = \boldsymbol{\varepsilon}^{e} + \boldsymbol{\varepsilon}^{of} + \boldsymbol{\varepsilon}^{co} + \boldsymbol{\varepsilon}^{vp} \tag{3.1}$$

in terms of the stress producing elastic strain $\boldsymbol{\varepsilon}^{e}$, the offset strain $\boldsymbol{\varepsilon}^{of}$, the coating strain $\boldsymbol{\varepsilon}^{co}$ and the viscoplastic strain $\boldsymbol{\varepsilon}^{vp}$. Here, the offset strains consider geometric tolerances discussed in Section 3.1 and the coating strain models a non-linear initial transition of the porous coating layer in Section 2.3.

3.3 Elastic response

The specific free energy for anisotropic elasticity is assumed to depend on the stress producing strain

$$\psi(\boldsymbol{\varepsilon}^{e}) = \frac{1}{2}\boldsymbol{\varepsilon}^{e} : \mathbb{C} : \boldsymbol{\varepsilon}^{e} \tag{3.2}$$

based on the elasticity tensor which has minor and major symmetries $\mathbb{C}_{ijkl} = \mathbb{C}_{klij} = \mathbb{C}_{jikl} = \mathbb{C}_{ijlk}$. Exploitation of the dissipation inequality $\mathcal{D} = \boldsymbol{\sigma} : \dot{\boldsymbol{\varepsilon}} - \dot{\psi} \geq 0$ motivates the stress definition

$$\boldsymbol{\sigma} = \frac{\partial \psi}{\partial \boldsymbol{\varepsilon}^{e}} = \mathbb{C} : \boldsymbol{\varepsilon}^{e} \tag{3.3}$$

and the reduced form of the dissipation inequality

$$\mathcal{D} = \boldsymbol{\sigma} : \dot{\boldsymbol{\varepsilon}}^{of} + \boldsymbol{\sigma} : \dot{\boldsymbol{\varepsilon}}^{co} + \boldsymbol{\sigma} : \dot{\boldsymbol{\varepsilon}}^{vp} \geq 0 \tag{3.4}$$

that must be fulfilled for all deformation states. For subsequent analysis, we restrict ourselves to orthotropic elasticity, which takes the following form in Voigt notation

$$\mathbb{C} = \begin{bmatrix} \mathbb{C}_{11} & \mathbb{C}_{12} & \mathbb{C}_{13} & 0 & 0 & 0 \\ \mathbb{C}_{12} & \mathbb{C}_{22} & \mathbb{C}_{23} & 0 & 0 & 0 \\ \mathbb{C}_{13} & \mathbb{C}_{23} & \mathbb{C}_{33} & 0 & 0 & 0 \\ 0 & 0 & 0 & \mathbb{C}_{44} & 0 & 0 \\ 0 & 0 & 0 & 0 & \mathbb{C}_{55} & 0 \\ 0 & 0 & 0 & 0 & 0 & \mathbb{C}_{66} \end{bmatrix} . \tag{3.5}$$

3.4 Evolution of offset and coating strain

For the offset strain, representing the tolerances in the height dimension, we assume

$$\boldsymbol{\varepsilon}^{of} = \varepsilon^{of} \boldsymbol{N}^{of} \qquad \text{with} \qquad \boldsymbol{N}^{of} = \boldsymbol{e}_z \otimes \boldsymbol{e}_z \tag{3.6}$$

where $\boldsymbol{e}_z$ represents a unit normal basis vector in the out-of-plane direction, i.e., the direction of tolerances. The amount of compressive offset strain follows by

$$\varepsilon^{of} = \begin{cases} \tilde{\varepsilon}^{of}(\boldsymbol{\varepsilon}, \boldsymbol{\varepsilon}^{co}, \boldsymbol{\varepsilon}^{vp}) & \text{for } \tilde{\varepsilon}^{of}(\boldsymbol{\varepsilon}, \boldsymbol{\varepsilon}^{co}, \boldsymbol{\varepsilon}^{vp}) \leq \varepsilon^{of}_{tol}, \\ \varepsilon^{of}_{tol} & \text{otherwise.} \end{cases} \tag{3.7}$$

where the parameter $\varepsilon^{of}_{tol} < 0$ takes into account the geometric tolerances in the interconnect contact heights. The offset function considers inelastic deformations in the soft coating layer and visco-plastic deformations in the metal interconnect that may have occured in the loading history

$$\tilde{\varepsilon}^{of}(\boldsymbol{\varepsilon}, \boldsymbol{\varepsilon}^{co}, \boldsymbol{\varepsilon}^{vp}) = (\boldsymbol{\varepsilon} - \boldsymbol{\varepsilon}^{co} - \boldsymbol{\varepsilon}^{vp}) : \boldsymbol{N}^{of} \tag{3.8}$$

Besides the offset strain correction, a coating strain is introduced that mimics the influence of a soft porous coating material. Analogous to equation (3.6) we assume

$$\boldsymbol{\varepsilon}^{co} = \varepsilon^{co} \boldsymbol{N}^{co} \qquad \text{with} \qquad \boldsymbol{N}^{co} = \boldsymbol{e}_z \otimes \boldsymbol{e}_z \tag{3.9}$$

where $\boldsymbol{e}_z$ represents a unit normal basis vector in the out-of-plane direction (or direction of tolerance). The amount of compressive coating strain is governed by

$$\varepsilon^{co} = \min_{\tau \in [0,t]} \tilde{\varepsilon}^{co}_{\tau} \tag{3.10}$$

and can be regarded as a minimum equivalent strain measure obtained in a typical, possibly non-monotonic loading process. For the equivalent strain measure for the soft coating material we assume

$$\tilde{\varepsilon}^{co}(\boldsymbol{\varepsilon}) = -a \left(1 - \exp\left[b\left(\boldsymbol{\varepsilon} : \boldsymbol{N}^{co} - \varepsilon^{of}_{tol}\right)\right]\right) \tag{3.11}$$

in terms of the material constants a and b.

3.5 Viscoplastic response

The evolution of the viscoplastic strain is assumed to have the following form

$$\dot{\boldsymbol{\varepsilon}}^{vp} = \dot{\varepsilon}^{vp} \boldsymbol{N}^{vp} \qquad \text{with} \qquad \boldsymbol{N}^{vp} = \mathbb{M} : \boldsymbol{\sigma}. \tag{3.12}$$

Here, the direction of anisotropic viscoplastic flow is governed by the Hill-type fourth order tensor $\mathbb{M}$ with the major and minor symmetries $\mathbb{M}_{ijkl} = \mathbb{M}_{klij} = \mathbb{M}_{jikl} = \mathbb{M}_{ijlk}$. Accoring to Xue & Hutchinson [9], a dependence of the effective stress on the hydrostatic stress components is considered by a Hill-type tensor which, in Voigt notation, takes the form

$$\mathbb{M} = \begin{bmatrix} \alpha_{12}+\alpha_{13}+\alpha_{11} & -\alpha_{12} & -\alpha_{13} & 0 & 0 & 0 \\ -\alpha_{12} & \alpha_{23}+\alpha_{12}+\alpha_{22} & -\alpha_{23} & 0 & 0 & 0 \\ -\alpha_{13} & -\alpha_{23} & \alpha_{13}+\alpha_{23}+\alpha_{33} & 0 & 0 & 0 \\ 0 & 0 & 0 & 6\,\alpha_{44} & 0 & 0 \\ 0 & 0 & 0 & 0 & 6\,\alpha_{55} & 0 \\ 0 & 0 & 0 & 0 & 0 & 6\,\alpha_{66} \end{bmatrix}. \tag{3.13}$$

The amount of viscoplastic flow is governed by

$$\dot{\varepsilon}^{vp} = \frac{\dot{E}_0}{\sigma_0} \left(\frac{\|\sigma\|_{\mathbb{M}}}{\sigma_0}\right)^{n-1} \qquad \text{with} \qquad \|\sigma\|_{\mathbb{M}} = \sqrt{\frac{1}{2}\boldsymbol{\sigma} : \mathbb{M} : \boldsymbol{\sigma}} \tag{3.14}$$

in terms of the material parameters $\dot{E}_0$, σ_0 and n. Incompressible isotropic plastic flow is recovered for $\mathbb{M} = \mathbb{P}$ with the fourth order deviatoric projection tensor $\mathbb{P} = \mathbb{I} - \frac{1}{3}\mathbf{1} \otimes \mathbf{1}$ and the fourth order identity tensor $\mathbb{I}_{ijkl} = \frac{1}{2}(\delta_{ik}\delta_{jl} + \delta_{jk}\delta_{il})$.

3.6 Effective model behavior

In this Section, the mechanical behavior of the effective model is discussed for several loading cases. To this end, a block geometry with dimensions identical to the high-fidelity RVE-model, i.e., 1.272 mm x 1.272 mm x 0.27 mm, is investigated using nominal material parameters. A compressive strain rate of $0.3s^{-1}$ was applied in the out-of-plane direction and a tensile strain rate of $0.008s^{-1}$ was applied in the in-plane direction. The geometry was discretized using one C3D8 element and uniaxial and biaxial loading states are applied to explain the main model characteristics. The material model was first tested for the offset formulation, with and without coating behavior, under uniaxial compression in the out-of-plane direction. The stress-strain response for this test is plotted in Figure 5(a). For the pure offset formulation, it is seen that, despite there being some strain in the element, the stress response ($\sigma_{zz}^{w/o\ co}$) is zero until a limiting strain threshold of about $\varepsilon_{zz} = 0.12$. When the strain in the element exceeds this threshold value, the material shows a typical elastoplastic response. For the offset and coating formulation, the stress response ($\sigma_{zz}^{w/\ co}$) can be characterized with a smooth exponential transition into the elastic domain and is also plotted in Figure 5(a). The effect of the offset and coating formulation for a uniaxial loading

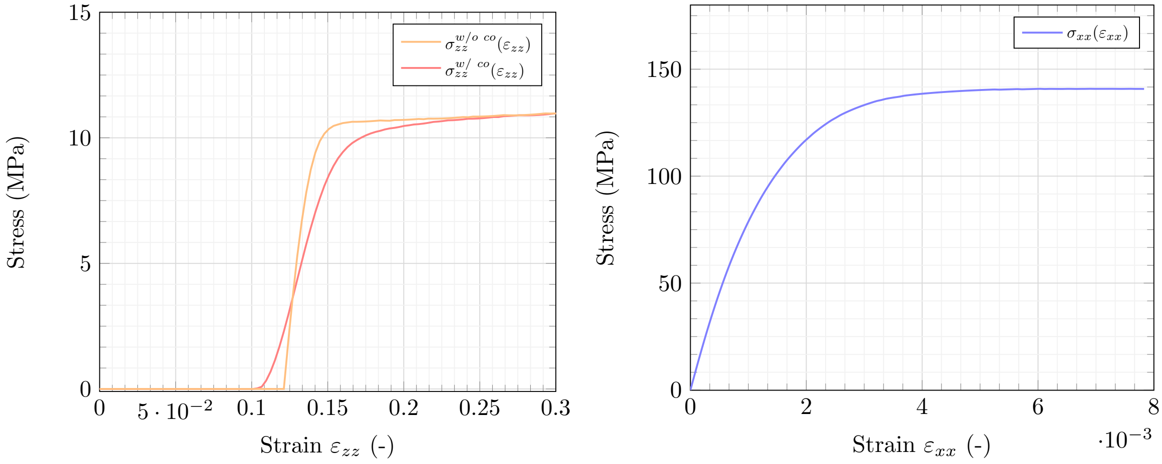

(a) Monotonic uniaxial out-of-plane load ε_{zz}.

(b) Monotonic uniaxial in-plane load ε_{xx}.

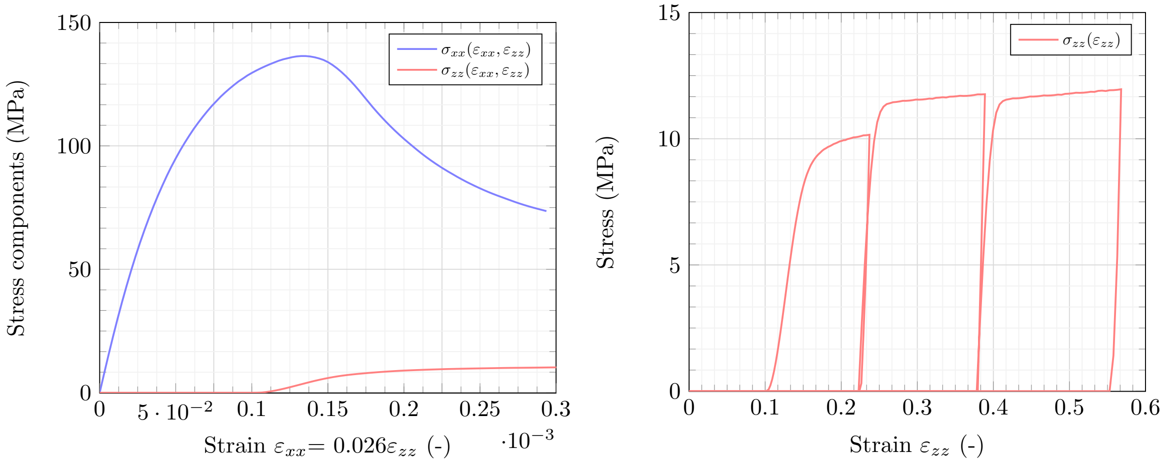

(c) Biaxial in-plane (ε_{xx}, ε_{yy}) and out-of-plane (ε_{xx}, ε_{zz}) load.

(d) Cyclic uniaxial out-of-plane load.

Figure 5: Characteristics of effective model: Offset and coating formulation under several loading cases.

in the in-plane direction is seen in Figure 5(b). The offset or coating parameters do not influence the in-plane behavior for a uniaxial loading case suggesting that the formulation developed in Section 3.4 does not cause any unforeseen effects in other directions for the uniaxial loading case. The offset and coating formulation was then tested using the same geometry under a normal loading in-plane and out-of-plane simultaneously with the mentioned strain rates. Figure 5(c) shows the stress-strain response over time for the in-plane and out-of-plane directions. In the offset domain, stress response in the in-plane direction is same as the uniaxial case in Figure 5(b). However, at the end of the offset domain, there is a decrease in the yield stress which depict a typical biaxial loading behavior. This infers that the loading in the offset domain gives a stress response equivalent to the uniaxial loading case in the in-plane direction. But when the strains exceed the offset threshold, the model shows a typical biaxial loading stress response. The loading-unloading behavior was plotted in Figure 5(d) for a uniaxial loading in the out-of-plane direction for three consecutive cycles. It was observed that there was a recovery of the elastic strain after each cycle, however, the offset-strain, coating-strain and plastic-strain was non-recoverable at zero stresses. It may also be noted that this formulation permits only compressive loading in the out-of-plane direction.

4 Computational investigations and validation

4.1 Parameter identification for effective model

The effective model was calibrated to the homogenized responses obtained in Section 2.3 for a steady state strain rate of 0.25 s^{-1} out-of-plane and 0.03 s^{-1} in-plane. Figure 6(d) shows the effective stress-strain response of uniaxial normal loading for a tall and short contact in the out-of-plane direction fitted on to its homogenized response. Figures 6(a), 6(b) and 6(c) show the fitting of the effective model for remaining normal and shear cases in-plane and out-of-plane. Similarly, the volume dilation for uniaxial normal loading cases in-plane and out-of-plane are also seen in Figure 6. Figure 6(e) shows the effective strain components $\varepsilon_{yy}(\varepsilon_{xx})$ and $\varepsilon_{zz}(\varepsilon_{xx})$ fitted onto the high fidelity homogenized model for a normal in-plane loading ε_{xx}. Figure 6(f) shows the effective strain components $\varepsilon_{xx}(\varepsilon_{zz})$ and $\varepsilon_{yy}(\varepsilon_{zz})$ fitted onto the high fidelity homogenized model for a normal out-of-plane loading ε_{zz}. The input properties for the effective model consists of an elasticity tensor $\mathbb{C}$, a plasticity tensor $\mathbb{M}$ and the viscoplastic coefficients $\dot{\epsilon}_0$, σ_0 and n, the limiting offset strain ϵ^{of}_{tol} and the coefficients for the coating strain a and b. Table 3 summarizes the identified anisotropic elastic and viscoplastic coefficients. Parameters for the viscoplastic

Table 3: Anisotropic input parameters for the effective model obtained from fit to homogenized response.

(a) Elasticity.

Elastic coefficients (MPa)	
$\mathbb{C}_{11}$	52000
$\mathbb{C}_{12}$	0
$\mathbb{C}_{13}$	0
$\mathbb{C}_{22}$	52000
$\mathbb{C}_{23}$	0
$\mathbb{C}_{33}$	650
$\mathbb{C}_{44}$	10000
$\mathbb{C}_{55}$	750
$\mathbb{C}_{66}$	750

(b) Viscoplasticity.

Hill-type coefficients (-)	
α_{11}	48.5
α_{12}	-19.5
α_{13}	0
α_{22}	200
α_{23}	0
α_{33}	3475
α_{44}	33.33
α_{55}	$408.33(tc), 466.667(sc)$
α_{66}	$408.33(tc), 466.667(sc)$

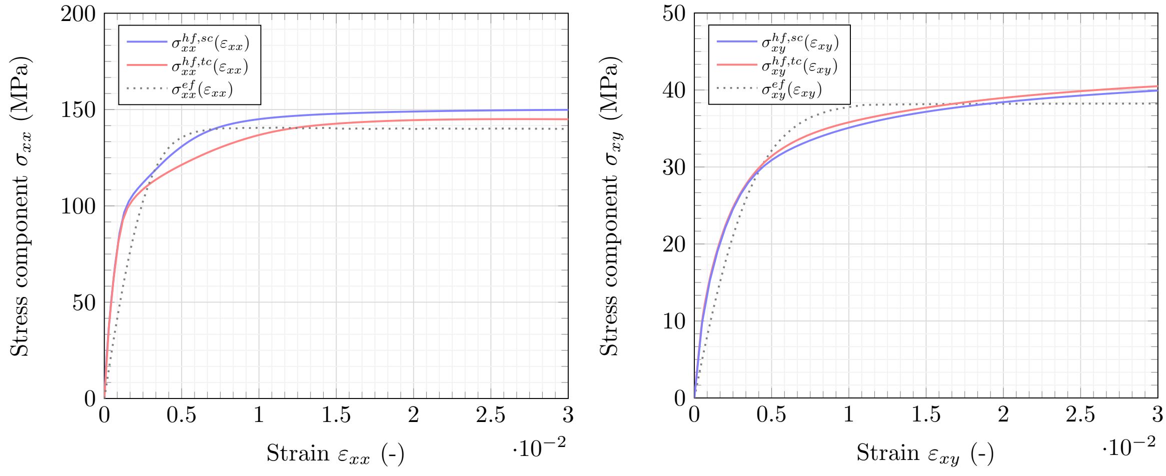

(a) In-plane normal

(b) In-plane shear

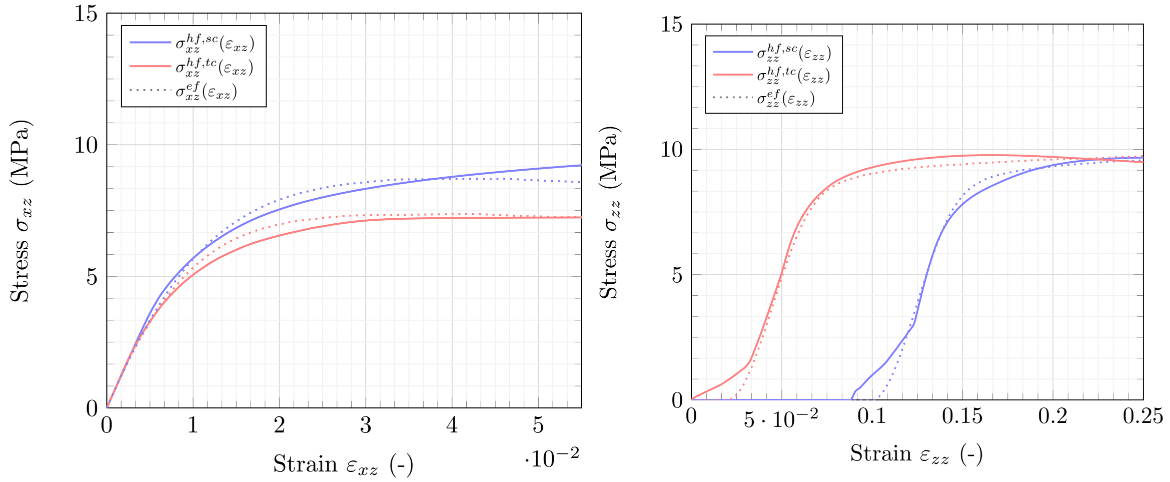

(c) Out-of-plane shear

(d) Out-of-plane normal

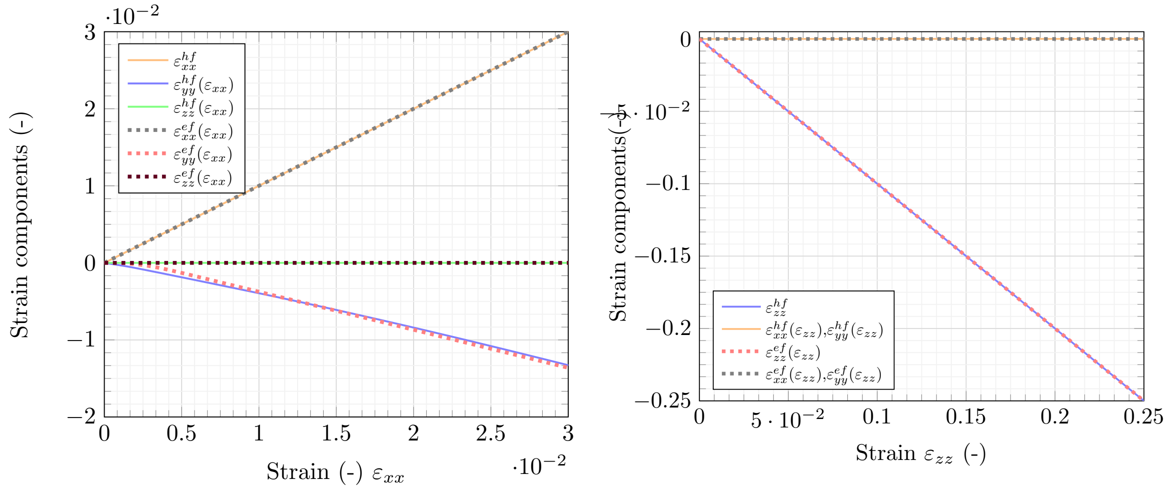

(e) Volume dilation (ε_{xx},ε_{yy}) for uniaxial normal in-plane loading (ε_{xx})

(f) Volume dilation (ε_{xx},ε_{yy}) for uniaxial normal out-of-plane loading (ε_{zz})

Figure 6: Parameter identification based on four basic deformation modes and volume dilation.

Table 4: Input parameters for the effective model obtained from fit to homogenized response.

(a) Viscoplasticity.

Initial strain rate (-)	
$\dot{\epsilon}_0$	0.00253602
Initial stress (MPa)	
σ_0	244.81
Exponent (-)	
n	1.55

(b) Tall contact.

Offset strain (-)	
$\varepsilon_{tol}^{of,tc}$	0.02
Coating thickness (mm)	
a^{tc}	0.04
Coating stiffness (MPa)	
b^{tc}	26.0

(c) Short contact.

Offset strain (-)	
$\varepsilon_{tol}^{of,sc}$	0.11
Coating thickness (mm)	
a^{sc}	0.04
Coating stiffness (MPa)	
b^{sc}	26.0

response and parameters for the offset and coating strain parameters for the tall and short contact are summarized in Table 4.

4.2 1-Layer: 16 Contacts

In order to validate the material model in Section 3, the effective model was compared to a high-fidelity simulation. The two coated contacts introduced and homogenized in Section 3.1 were used to create a grid of 16 contacts of 2 different height dimensions. Their heights were 25 μm apart and were positioned at random locations in the grid. An effective model was constructed replacing the contacts by brick elements as discussed in Section 3.6 with same positions of tall and short contacts. The material properties for the effective model was taken from Section 4.1. Both models were compressed between rigid plates with the strain rates given in Section 4.1 and were constrained in-plane at their edges. Figure 7(a) and Figure 7(b) show the stress concentration in the high-fidelity model and effective model in the $zz-direction$. The contacts with larger height dimension exhibited larger stress concentrations in the $zz-direction$ and upon undergoing deformation of about 25 μm, the shorter contacts began to deform. Figure 7(c) shows the force-displacement curves from the compression simulations and the curve fit closely. The effective model had a significantly reduced simulation time which was compared with the high-fidelity case. The high-fidelity model required 48 parallel CPUs on the high performance cluster and took about 28 hours whereas the effective model took about 30 seconds on a standard workstation desktop. This shows that the effective model is capable of successfully simulating variability in the height dimension of contacts on an SOC interconnect as well as non-linear coating behavior.

4.3 2-Layer: 16 Contacts

In the previous section, the effective model was validated for the compression of a single interconnect layer. In this section, the repeatibility of results for a multilayered stack was tested. The coated interconnect contacts of two height dimensions were used to create interconnects with a variability in its contact heights as discussed in Section 4.2. The height dimensions between the two contacts were 25 μm apart and were positioned at random locations. Two such interconnects were stacked together separating each other with rigid plates. The effective model was constructed in a similar way as discussed in Section 4.2. The material proprties for tall and short contacts and the loading condtions were taken from Section 4.2. Figure 7(d) and Figure 7(e) show the stress concentration in the high-fidelity model and effective model. Figure 7(f) shows the force-displacement curves from the compression simulations. It may be noted that on increasing the number of layers, the effective model consistently represents the high fidelity model.

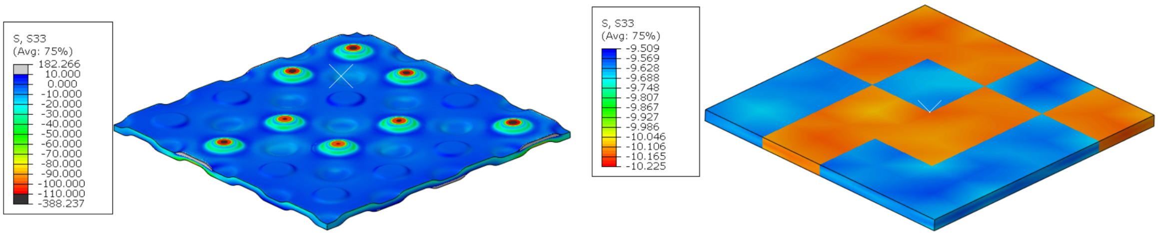

(a) High-fidelity model (b) Effective model

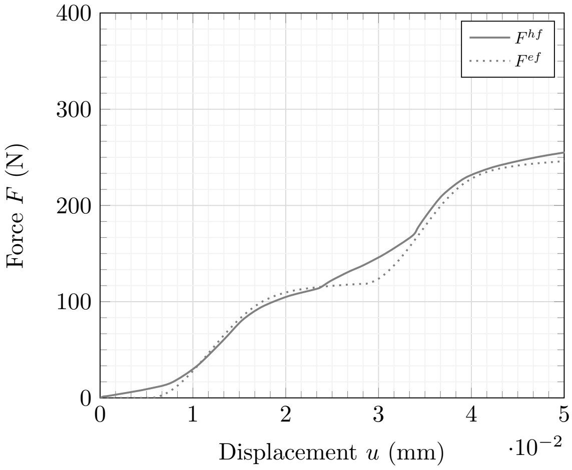

(c) Force-Displacement on 1-Layer: 16 contacts

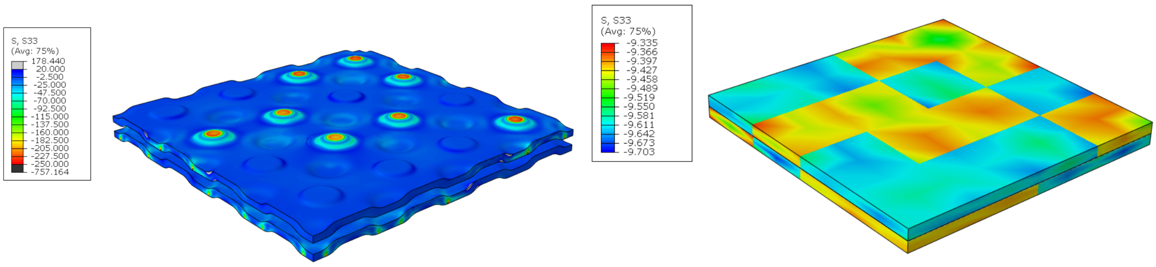

(d) High-fidelity model (e) Effective model

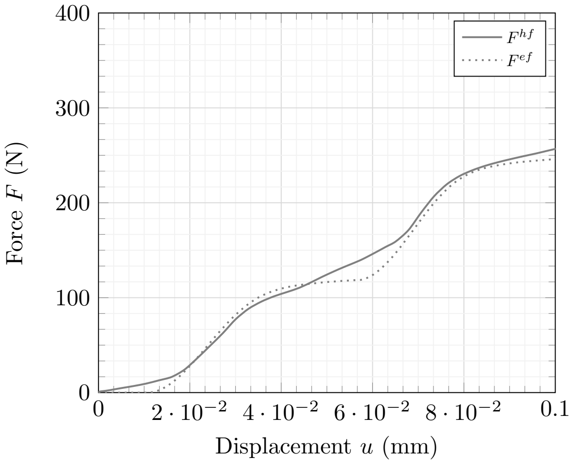

(f) Force-Displacement on 2-Layers: 16 contacts

Figure 7: Numerical Validation for 1-Layer and 2-Layers of interconnects

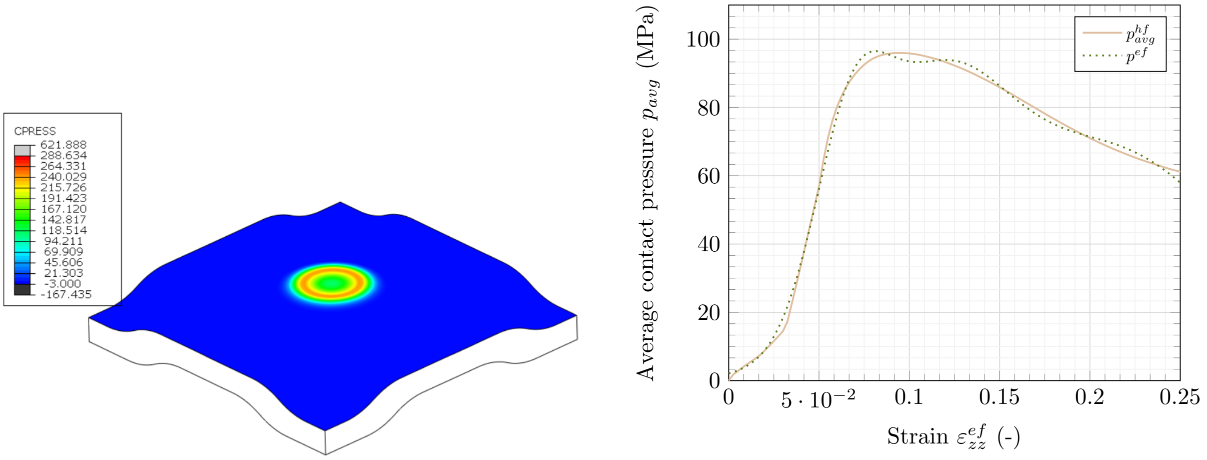

(a) Contact pressure p^{hf} in high fidelity simulation for one contact

(b) Fitting of contact pressure p^{ef} for effective model

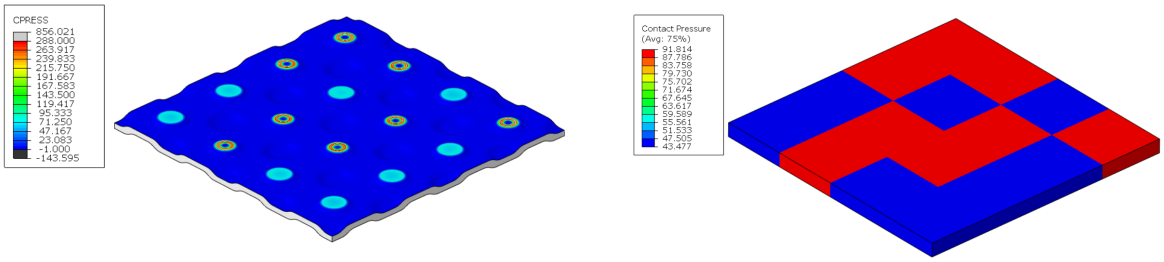

(c) Contact pressure p^{hf} in high fidelity simulation of 16 contacts

(d) Contact pressure p^{ef} in effective model of 16 contacts

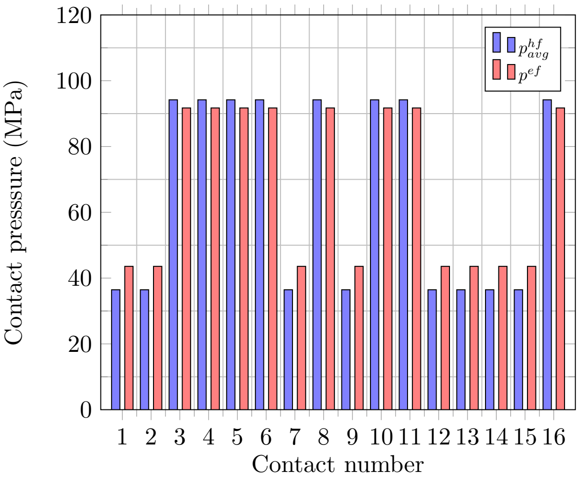

(e) Comparison of contact pressures in high fidelity p^{hf} and effective model p^{ef} at $218N$

Figure 8: Evaluation and validation of contact pressures at individual contacts in the high fidelity p^{hf} and effective model p^{ef}.

4.4 Evaluation of interconnect contact situation

In this section, a layout is described which uses this model in a setting specific to evaluation of contact pressure for SOC contacts, where the displacement, or the force, used to compress a stack is input to the effective model. At the end of a stack compression simulation, the contact situation of the interconnects is computed in a *post-processing step*. In the effective model, the effective strains $\boldsymbol{\varepsilon}^{ef} = \boldsymbol{\varepsilon} - \boldsymbol{\varepsilon}^{of}$ describe the effective compression of individual contacts. This strain is proportional to the contact pressure based on a relation which may be derived from previously executed high-fidelity FEM compression simulation. The resulting average contact pressure versus effective strain relation is obtained from a high-fidelity FEM compression simulation for one contat which expresses the average contact pressure as a function of effective strain $\boldsymbol{\varepsilon}^{ef}$ and can predict the average contact pressure directly from the effective model. In this layout, the average contact pressure for the compression of a single contact is evaluated from the simulation depicted in Figure 8(a). The average contact pressure is plotted versus the strain in the RVE. This relation is shown in Figure 8(b). Aiming at an efficient estimation of the contact pressure based on simulations with the effective model, the following relation is assumed in Equation 4.1.

$$p^{ef} = k_1 \, \exp\left[-\left(\frac{\varepsilon_{zz}^{ef} - k_2}{k_3}\right)^2\right] + k_4 \, \exp\left[-\left(\frac{\varepsilon_{zz}^{ef} - k_5}{k_6}\right)^2\right] + k_7 \, \exp\left[-\left(\frac{\varepsilon_{zz}^{ef} - k_8}{k_9}\right)^2\right] \tag{4.1}$$

The coefficients for Equation 4.1 obtained from a curve fitting routine are summarized in Table 5. Using these parameters, the fitted function in Equation 4.1 is plotted in Figure 8(b). This relation represents the average contact pressure as a function of the effective strain $\boldsymbol{\varepsilon}^{ef}$ of each contact, obtained from the effective model. The average contact pressure at each contact can be evaluated in the high fidelity model in Figure 8(c) and compared with the contact pressures evaluated from effective strains $\boldsymbol{\varepsilon}^{ef}$ in the effective model in Figure 8(d). At a nominal stacking force of about $218N$, the distribution of contact pressures at each contact is compared for the high fidelity model and the effective model in Figure 8(e).

Table 5: Input parameters for estimation of contact pressure from effective model response.

Contact pressure coefficients (-)	
k_1	46.83
k_2	0.06711
k_3	0.02851
k_4	63.51
k_5	0.1118
k_6	0.05506
k_7	67.28
k_8	0.2106
k_9	0.1014

5 Conclusion

Dimensional tolerances at interconnect contacts cause inefficient contacting and affect SOC stack performance. The work prewented here primarily focuses on creating the necessary tools in the finite element framework to understand the influence of these tolerances (particularly height tolerance) during stack pressing. Due to large computation time of high-fidelity models, the homogenization approach was used to simulate interconnect contacts with different height dimensions for their stress-strain responses. A rate-dependent compressible anisotropic elastoplastic effective model was developed and fit to the homogenized stress-strain responses for contacts of two different dimensions. This work introduced the concept of *offset strain* in an anisotropic framework to model dimensional tolerances. Subsequently, this concept was extended to model non-linear behaviors, such as coatings on metallic interconnects. The necessary mathematical framework was formulated, coded using Intel FORTRAN and implemented in ABAQUS through user material subroutine (UMAT). Finally, the effective model was validated using a benchmark, high-fidelity simulation. The model used for this study had a specific interconnect design, however, this approach may be generalized for any design (for example, a channel type sinusoidal interconnect design). The idea of offset-strains can be used for other elastoplastic models and the exponential coating behavior may also be replaced with a different function for materials with a peculiar behavior in any specific direction. However, it should be noted that these equations may not work well for isotropic models without introducing a certain level of anisotropy. An isotropic update of offset-strains would introduce in-plane instability because of the in-plane offset formulation. With a general anisotropic elastoplastic model (with plastic incompressibility), the offset strains show a good convergence at low variability in height dimensions. However, for larger variability, elements with different offset-strains see plasticity at different instances. This introduces plastic incompressibility in-plane at different rates which may cause element distortion. One could set the elastic Poisson's ratio to get isochoric behavior in the elastic domain, so with the onset of plasticity, the in-plane expansion for all elements are at the same rate, avoiding distortion. This was tested by adapting the formulation to different anisotropic plasticity algorithms like Miehe et al. [18, 19] to check its applicability for further use. Contact pressure is a very important parameter while studying performance of fuel cells. Therefore, in the last part of this paper, a layout is provided to convert the parameters obtained from the effective model in terms of contact pressure. To use this model in practice, the height tolerance data on several interconnects may be measured using some kind of measurment setup. An effective stack model uses this data along with the stack pressing force (or displacement) as input and calculates effective strains at individual contacts. The contact pressure can be expressed as a function of these strains as described in Section 4.4 and a quantitative estimation of the distribution of contact pressure can be obtained. Finally, the stacking forces may be optimized for suitable contacting conditions while minimizing large plastic deformation.

Appendix A. Periodic boundary conditions for high-fidelity model

In this Section, the equation constraints for periodic boundary conditions are described for faces, edges and corners. u^{cd} is the key degree of freedom for the given direction. The two faces to be constrained are 'A' and 'B' used as superscripts. The principle normal and shear directions are xx, yy, zz, xy, xz, yz. u_x, u_y and u_z are the displacement components in all directions. Δl is the distance between the two faces. The constraint equation for the two faces take the form

$$\begin{aligned} u_x^A - u_x^B - u_{xx}^{cd}\Delta l &= 0 \\ u_y^A - u_y^B - u_{xy}^{cd}\tfrac{1}{2}\Delta l &= 0 \\ u_z^A - u_z^B - u_{xz}^{cd}\tfrac{1}{2}\Delta l &= 0 \end{aligned} \tag{5.1}$$

The equations for the other six faces can be written following a similar pattern and is not mentioned here. The edges parallel to the z-axis are labelled as I, II, III and IV. Edge I is taken as the reference edge and edge II is adjacent to it on the x-axis, so the equations for these edges take the form

$$
\begin{aligned}
u_x^{II} - u_x^{I} - u_{xx}^{cd}\Delta l &= 0\\
u_y^{II} - u_y^{I} - u_{xy}^{cd}\tfrac{1}{2}\Delta l &= 0\\
u_z^{II} - u_z^{I} - u_{xz}^{cd}\tfrac{1}{2}\Delta l &= 0
\end{aligned}
\tag{5.2}
$$

Edge IV is adjacent to edge I on the y-axis (2-direction) and the equations take the form

$$
\begin{aligned}
u_x^{IV} - u_x^{I} - u_{xy}^{cd}\tfrac{1}{2}\Delta l &= 0\\
u_y^{IV} - u_y^{I} - u_{yy}^{cd}\Delta l &= 0\\
u_z^{IV} - u_z^{I} - u_{yz}^{cd}\tfrac{1}{2}\Delta l &= 0
\end{aligned}
\tag{5.3}
$$

The equations for edge III diagonally opposite to edge I can be written as a combination of edges II and IV in the form

$$
\begin{aligned}
u_x^{IV} - u_x^{I} - u_{xx}^{cd}\Delta l - u_{xy}^{cd}\tfrac{1}{2}\Delta l &= 0\\
u_y^{IV} - u_y^{I} - u_{xy}^{cd}\tfrac{1}{2}\Delta l - u_{yy}^{cd}\Delta l &= 0\\
u_z^{IV} - u_z^{I} - u_{xz}^{cd}\tfrac{1}{2}\Delta l - u_{yz}^{cd}\tfrac{1}{2}\Delta l &= 0
\end{aligned}
\tag{5.4}
$$

The equations for other edges parallel to the x-axis and y-axis can be written using the same pattern. For corners, one reference corner is identified and the equations for all other corners are formulated with reference to the position of this corner. The reference corner is labeled with superscript 'ref' and the adjacent corner with superscript 'adj'. For this case, the corner is adjacent in the x-direction

$$
\begin{aligned}
u_x^{ref} - u_x^{adj} - u_{xx}^{cd}\Delta l &= 0\\
u_y^{ref} - u_y^{adj} - u_{xy}^{cd}\tfrac{1}{2}\Delta l &= 0\\
u_z^{ref} - u_z^{adj} - u_{xz}^{cd}\tfrac{1}{2}\Delta l &= 0
\end{aligned}
\tag{5.5}
$$

The diagonal corners are expressed as a combination of multiple adjacent corners as done for the edges. Using this pattern, the equations for all other corners can be written. For a more detailed understanding, the reader could refer to a thesis by Praud [20].

Appendix B. Algorithmic treatment of model equations

The constitutive equations for the effective model, see Section 3, are implemented into the commercial finite element package ABAQUS [21] using the user material model interface UMAT. In a typical time-stepping procedure we consider the process interval $[0, T]$. In this interval we are seeking the solutions at the discete times $0, t_1, t_2, \ldots, t_n, t_{n+1}, \ldots, T$ where all field variables at time t_n are assumed to be known. Aiming at a compact notation, we drop in what follows the subscript t_{n+1} and consider all variables without subscript to be evaluated at time t_{n+1}. In a time discrete setting, the stresses are computed via

$$
\boldsymbol{\sigma} = \mathbb{C} : \boldsymbol{\varepsilon}^{e} = \mathbb{C} : [\boldsymbol{\varepsilon} - \boldsymbol{\varepsilon}^{of}(\boldsymbol{\varepsilon}, \boldsymbol{\varepsilon}_n^{co}, \boldsymbol{\varepsilon}_n^{vp}) - \boldsymbol{\varepsilon}^{co}(\boldsymbol{\varepsilon}) - \boldsymbol{\varepsilon}^{vp}(\boldsymbol{\sigma}(\boldsymbol{\varepsilon}))]
\tag{5.6}
$$

In a time discrete setting, the algorithmic counterpart of the offset strain formulation (3.8) reads

$$
\varepsilon^{of} = \begin{cases} \tilde{\varepsilon}^{of}(\boldsymbol{\varepsilon}, \boldsymbol{\varepsilon}_n^{co}, \boldsymbol{\varepsilon}_n^{vp}) & \text{for } \tilde{\varepsilon}^{of}(\boldsymbol{\varepsilon}, \boldsymbol{\varepsilon}_n^{co}, \boldsymbol{\varepsilon}_n^{vp}) \leq \varepsilon_{tol}^{of},\\ \varepsilon_{tol}^{of} & \text{otherwise.} \end{cases}
\tag{5.7}
$$

in terms of the time-discrete equivalent offset strain function

$$
\tilde{\varepsilon}^{of}(\boldsymbol{\varepsilon}, \boldsymbol{\varepsilon}_n^{co}, \boldsymbol{\varepsilon}_n^{vp}) = (\boldsymbol{\varepsilon} - \boldsymbol{\varepsilon}_n^{co} - \boldsymbol{\varepsilon}_n^{vp}) : \boldsymbol{N}^{of}
\tag{5.8}
$$

in which a semi-implicit approach was chosen for the dependencies on the coating and viscoplastic strains. Similarly, the update of the amount of coating strain (3.10) follows by

$$\varepsilon^{co} = \begin{cases} \tilde{\varepsilon}^{co}(\boldsymbol{\varepsilon}) & \text{for } \tilde{\varepsilon}^{co}(\boldsymbol{\varepsilon}) \leq \varepsilon^{co}_n, \\ \varepsilon^{co}_n & \text{otherwise.} \end{cases} \tag{5.9}$$

where the irreversibility constraint for the coating strain is considered explicitely. The equivalent strain measure for the soft coating material reads

$$\tilde{\varepsilon}^{co}(\boldsymbol{\varepsilon}) = -a\left(1 - \exp\left[b\left(\boldsymbol{\varepsilon} : \boldsymbol{N}^{co} - \varepsilon^{of}_{tol}\right)\right]\right). \tag{5.10}$$

The time-discrete counterpart of the evolution equation for the viscoplastic strain update (3.12) reads

$$\Delta\boldsymbol{\varepsilon}^{vp} = \Delta t \lambda(\boldsymbol{\sigma})\, \mathbb{M} : \boldsymbol{\sigma} \qquad \text{with} \qquad \lambda(\boldsymbol{\sigma}) = \frac{\dot{E}_0}{\sigma_0}\left(\frac{\sigma^{eq}}{\sigma_0}\right)^{n-1} \qquad \text{and} \qquad \sigma^{eq} = \sqrt{\frac{1}{2}\boldsymbol{\sigma} : \mathbb{M} : \boldsymbol{\sigma}}. \tag{5.11}$$

Reformulation of the stress update in equation (5.6) gives

$$\boldsymbol{\sigma} = \boldsymbol{\sigma}^{tr} - \mathbb{C} : \Delta\boldsymbol{\varepsilon}^{vp}(\boldsymbol{\sigma}) \qquad \text{with} \qquad \boldsymbol{\sigma}^{tr} = \mathbb{C} : [\boldsymbol{\varepsilon} - \boldsymbol{\varepsilon}^{of}(\boldsymbol{\varepsilon}, \boldsymbol{\varepsilon}^{co}_n, \boldsymbol{\varepsilon}^{vp}_n) - \boldsymbol{\varepsilon}^{co}(\boldsymbol{\varepsilon}) - \boldsymbol{\varepsilon}^{vp}_n]. \tag{5.12}$$

where we introduced the trial stresses as a function of the total current strain and the coating and offset strains evaluated at In a residual format we obtain the nonlinear equation for the stresses

$$\boldsymbol{r}(\boldsymbol{\sigma}) := \boldsymbol{\sigma} - \boldsymbol{\sigma}^{tr} + \Delta t\, \lambda(\boldsymbol{\sigma})\, \mathbb{C} : \mathbb{M} : \boldsymbol{\sigma}. \tag{5.13}$$

This equation is solved using Newtons method with the following stress update

$$\boldsymbol{\sigma} \Leftarrow \boldsymbol{\sigma} + \Delta\boldsymbol{\sigma} \qquad \text{with} \qquad \Delta\boldsymbol{\sigma} = -\boldsymbol{r}(\boldsymbol{\sigma}) : \left[\frac{\partial \boldsymbol{r}}{\partial \boldsymbol{\sigma}}\right]^{-1} \tag{5.14}$$

until convergence is obtained in the sense of $\|\boldsymbol{r}(\boldsymbol{\sigma})\| \leq tol$. The required tangent reads

$$\frac{\partial \boldsymbol{r}}{\partial \boldsymbol{\sigma}} = \mathbb{I}^s + \Delta t\left[\frac{\partial \lambda}{\partial \sigma^{eq}} \mathbb{M} : \boldsymbol{\sigma} \otimes \mathbb{C} : \mathbb{M} : \boldsymbol{\sigma} + \lambda\, \mathbb{C} : \mathbb{M}\right] \qquad \text{with} \qquad \frac{\partial \lambda}{\partial \sigma^{eq}} = \frac{(n-1)\dot{E}_0}{\sigma_0^2}\left(\frac{\sigma^{eq}}{\sigma_0}\right)^{n-2}. \tag{5.15}$$

If convergence of the local Newton iteration has been achieved, the viscoplastic strain can be updated

$$\boldsymbol{\varepsilon}^{vp} = \boldsymbol{\varepsilon}^{vp}_n + \Delta t\, \lambda(\boldsymbol{\sigma})\, \mathbb{M} : \boldsymbol{\sigma} \tag{5.16}$$

and the material tangent, required in a finite element context, can be calculated

$$\frac{\partial \boldsymbol{\sigma}}{\partial \boldsymbol{\varepsilon}} = \mathbb{C} : \left[\mathbb{I}^s - \frac{\partial \boldsymbol{\varepsilon}^{of}}{\partial \boldsymbol{\varepsilon}} - \frac{\partial \boldsymbol{\varepsilon}^{co}}{\partial \boldsymbol{\varepsilon}}\right] : \left[\frac{\partial \boldsymbol{r}}{\partial \boldsymbol{\sigma}}\right]^{-1} \tag{5.17}$$

containing the derivatives related to the offset and coating strains

$$\frac{\partial \boldsymbol{\varepsilon}^{of}}{\partial \boldsymbol{\varepsilon}} = \begin{cases} \boldsymbol{N}^{of} \otimes \boldsymbol{N}^{of} & \text{for } \tilde{\varepsilon}^{of}(\boldsymbol{\varepsilon}, \boldsymbol{\varepsilon}^{co}_n, \boldsymbol{\varepsilon}^{vp}_n) \leq \varepsilon^{of}_{tol}, \\ \mathbb{0} & \text{otherwise.} \end{cases} \tag{5.18}$$

and

$$\frac{\partial \boldsymbol{\varepsilon}^{co}}{\partial \boldsymbol{\varepsilon}} = \begin{cases} a\, b \exp\left[b\left(\boldsymbol{\varepsilon} : \boldsymbol{N}^{co} - \varepsilon^{of}_{tol}\right)\right] \boldsymbol{N}^{co} \otimes \boldsymbol{N}^{co} & \text{for } \tilde{\varepsilon}^{co}(\boldsymbol{\varepsilon}) \leq \varepsilon^{co}_n, \\ \mathbb{0} & \text{otherwise.} \end{cases} \tag{5.19}$$

Data availability

The data that support the findings of this study are available from the corresponding author upon reasonable request.

Conflict of interests

On behalf of all authors, the corresponding author states that there is no conflict of interest.

References

[1] Z. Wu, Y. Zhou, G. Lin, S. Wang, and J. Hub, "An improved model for predicting electrical contact resistance between bipolar plate and gas diffusion layer in proton exchange membrane fuel cells," *Journal of Power Sources*, vol. 182, pp. 265–269, 2008.

[2] M. Navasa, X.-Y. Miao, and H. L. Frandsen, "A fully-homogenized multiphysics model for a reversible solid oxide cell stack," *International Journal of Hydrogen Energy*, vol. 44, pp. 23330–23347, 2019.

[3] J. C. Simo and T. J. R. Hughes, *Computational Inelasticity.* Springer, 1998.

[4] J. Lemaitre and J.-L. Chaboche, *Mechanics of Solid Materials.* Cambridge University Press.

[5] T. T. Molla, K. Kwok, and H. L. Frandsen, "Efficient modeling of metallic interconnects for thermo-mechanical simulation of sofc stacks: Homogenized behaviors and effect of contact," *International Journal of Hydrogen Energy*, vol. 41, pp. 6433–6444, 2016.

[6] M. Tsuda, E. Takemura, T. Asada, N. Ohno, and T. Igari, "Homogenized elastic-viscoplastic behavior of plate-fin structures at high temperatures: Numerical analysis and macroscopic constitutive modeling," *International Journal of Mechanical Sciences*, vol. 52, pp. 648–656, 2010.

[7] J. Ulloa, R. Alessi, J. Wambacq, G. Degrande, and F. Stijn, "On the variational modeling of non-associative plasticity," *International Journal of Solids and Structures*, vol. 217–218, pp. 272–296, 2021.

[8] V. S. Deshpande and N. A. Fleck, "Isotropic constitutive models for metallic foams," *Journal of the Mechanics and Physics of Solids*, vol. 48, pp. 1253–1283, 2000.

[9] Z. Xue and J. W. Hutchinson, "Constitutive model for quasi-static deformation of metallic sandwich cores," *Composites: Part A*, vol. 61, pp. 2205–2238, 2004.

[10] J. H. Zhu and H. Ghezel-Ayagh, "Cathode-side electrical contact and contact materials for solid oxide fuel cell stacking: a review," *International Journal of Hydrogen Energy*, vol. 42, pp. 24278–24300, 2017.

[11] D. Kennouche, Q. Fang, L. Blum, and D. Stolten, "Analysis of the cathode electrical contact in sofc stacks," *Journal of The Electrochemical Society*, vol. 165, pp. 677–683, 2018.

[12] Ceres Intellectual Property Company Limited, WO 2020/1264S6 A1, *Fuel cell unit and fuel cell stack*, 2020.

[13] H. Abdoli, S. Molin, and H. Farnoush, "Effect of interconnect coating procedure on solid oxide fuel cell performance," *Materials Letters*, vol. 259, p. 126898, 2020.

[14] F. Shen, S. A. Ibanez, and M. C. Tucker, "Dynamic oxidation of (mn,co) 3o 4-coated interconnects for solid oxide electrolysis cells," *International Journal of Hydrogen Energy*, 2023.

[15] VDM Metals International GmbH, *Werkstoffdatenblatt Nr. 4146 VDM® Crofer 22 APU*, 2022.

[16] S. Li, N. Warrior, Z. Zou, and F. Almaskari, "A unit cell for fe analysis of materials with the microstructure of a staggered pattern," *Composites: Part A*, vol. 42, pp. 801–811, 2011.

[17] S. Li, "On the key degrees of freedom for unit cells obtained from periodic conditions and their significances in micromechanical fe analysis, in preparation," *t.b.d.*, vol. t.b.d., p. t.b.d., t.b.d.

[18] C. Miehe, N. Apel, and M. Lambrecht, "Anisotropic additive plasticity in the logarithmic strain space: modular kinematic formulation and implementation based on incremental minimization principles for standard materials," *Computer methods in applied mechanics and engineering*, vol. 191, pp. 5383–5425, 2002.

[19] C. Miehe, J. Schotte, and M. Lambrecht, "Homogenization of inelastic solid materials at finite strains based on incremental minimization principles. application to the texture analysis of polycrystals," *Journal of the Mechanics and Physics of Solids*, vol. 50, pp. 2123–2167, 2002.

[20] F. Praud, *Multi-scale modelling of thermoplastic-based woven composites, cyclic and time-dependent behaviour.* Phd thesis, l'École Nationale Supérieure d'Arts et Métiers, November 2018.

[21] Dassault Systèmes Simulia Corporation, *ABAQUS documentation*, 2021.